The AMADEUS Dextrous Subsea Hand: Design, Modeling, and Sensor Processing

David M. Lane, J. Bruce C. Davies, Graham Robinson, Desmond J. O'Brien,
Jim Sneddon, Euan Seaton, and Anders Elfstrom

Abstract—This paper describes the mechanical design, finger modeling, and sensor signal processing for a dextrous subsea robot hand incorporating force and slip contact sensing. The hand uses a fluid-filled tentacle for each finger, which has inherent passive compliance, and no moving parts. Force sensing uses strain gauges mounted in the fingertip, potted within a silicon elastomer. Slip sensing uses a piezoelectric strip to detect vibration, embedded 1 mm below the elastomer surface. Static models of finger motion are presented and validated based on bending moments and hydraulic pressure. The design of a stochastic estimator is also described, for sensor fusion of contact force magnitude and direction data, obtained using redundant strain gauges in the fingertip. Finally, linear dynamic models of the finger dynamics in contact with a rigid surface are obtained using least squares and recursive least squares parameter estimation, as a precursor to closed-loop force control during grasping.

Index Terms—Dextrous manipulator, flexible robot, force and slip sensing, robot hand, static and dynamic modeling, subsea.

I. INTRODUCTION

CURRENT generation subsea robots generally employ claw-like manipulator end effectors (see Fig. 1), capable only of open/close and wrist-rotate movements, with no sensing or control of contact forces. Attempts at object grasping often result in damage through unwitting application of excessive contact forces. T-bars and other attachments can be used on man-made objects but are prone to snapping when overloaded. Such damage introduces expensive delays or complete failure in task execution.

An analysis of requirements in benthic science and marine geology [1] has indicated that several kinds of sampling operation involving fragile objects would benefit if grasp forces and object deformation were controllable. Similarly, insertion tasks in offshore oil and gas tasks would be made easier if grasped object pose could be precisely tuned over a small range without moving the complete manipulator and/or vehicle. In both cases, low-force high-precision manipulation is needed, using dextrous movements of end effectors with feedback for control of contact forces and torques. For use
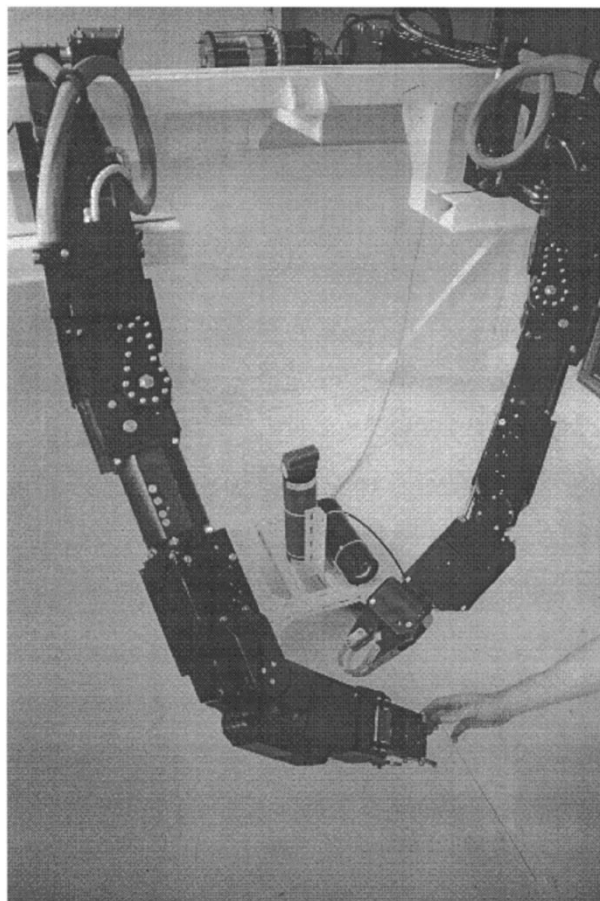
Fig. 1. Slingsby TA-9 hydraulic manipulators with typical claw end effectors.

in the ocean, construction must also be robust, reliable, and simple. Adaptations of existing in-air dextrous grippers may therefore be overly complex for subsea use [2].

Flexible *continuum robots* [3] offer attractive possibilities for use in the ocean. These devices produce movements by bending as an elastic continuum, without the need for an additional skeletal structure. They offer natural passive compliance to correct for inevitable positioning inaccuracies, with simplicity of design and a minimum of moving parts. They are therefore well suited to building dextrous grippers capable of reducing breakages and task execution delay/failure in low-force grasping and manipulation.

Although extensive work has been reported on control of robots containing flexible links [4], little has been reported on

flexible actuators. Early work [5] focused only on wrist design to avoid singularities. Latterly, [6]–[9] have all described flexible robot constructions with tendons. In [10], the design of a microactuator was described using differential pressure in fluid-filled rubber chambers.

This paper describes the design, modeling, and sensor signal processing for a hydraulically actuated subsea dextrous gripper using flexible fingers as actuators, building on early original work with pneumatic systems [11]–[15]. Finger bending is produced via the action of differential hydraulic pressures in three mechanically coupled flexible tubes. The gripper then consists of three fingers, each mounted on a knuckle mechanism to provide additional movement.

For subsea applications, contact sensing must be independent of ambient pressure. Suitable force and slip sensing techniques have therefore been designed and integrated within each fingertip to enable closed-loop control of finger force and hand grasp. Fingertip precision grasps [16] are used throughout.

Section II overviews the mechanical design of the gripper, and Section III presents static models of its motion based on bending moments and applied pressure. Section IV then presents the force and slip sensors and describes a stochastic estimation approach used to exploit redundancy in strain gauge data, thus obtaining improved estimates of force magnitude and direction during contact. Finally, Section V presents results estimating the dynamics of a finger in contact with a rigid surface, through application of off-line least squares and on-line recursive least squares system identification with linear second-order models.

II. MECHANICAL DESIGN

The gripper consists of three modular sections: body, finger, and finger tip (Fig. 2), with the hydraulic and control systems as separate units. The modular approach allows a range of components, materials, and geometries to be evaluated in the laboratory without extensive reworking of the entire gripper system, and follows sound underwater design principles [17].

A. Finger Design

The operation of the AMADEUS gripper fingers relies on the elastic deformation of cylindrical metal bellows with thin convoluted walls. The convolutions ensure that the assembly is significantly stiffer radially than longitudinally and that longitudinal extension is therefore much greater than radial expansion when subjected to internal pressure. Initially, phosphor bronze bellows (14.3-mm outside diameter (OD) and length 125 mm) with 52 active convolutions and 0.28-mm wall thickness are used.

Each finger is made up from three bellows placed in a parallel arrangement forming the vertices of an equilateral triangle (pitch center diameter (PCD) 30 mm). The proximal end of the triad is attached to the knuckle joint of the gripper body, the other to an end-plate, which connects each bellow to the other two members of a particular finger. Utilizing a different pressure in each bellow creates a range of extension forces causing the finger to bend according to the constraints
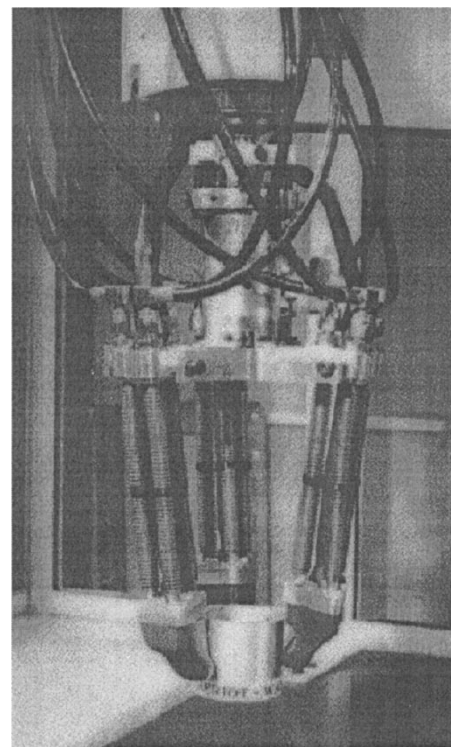
(a)
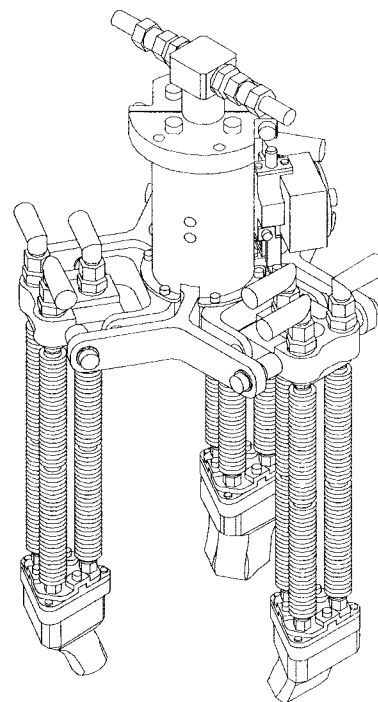
(b)

Fig. 2. AMADEUS phase I prototype gripper. (a) Hardware. (b) Schematic.

provided by the end plate (Fig. 3). The larger the differential pressure, the larger the resulting finger tip deflection. In addition to bending, the triangular arrangement enables the direction of finger tip movement to be controlled.

The potential advantages of this type of construction stem from the simplicity of the finger mechanism (there are no

Overall height (including fingers):	365 mm	Peak finger tip force (straight):	15.45 N
Mass (of gripper):	3.5 kg	Target object dimensions:	
Knuckle movement	±20°	(minimum):	∅10 mm
Finger deflection (maximum):	20mm	(maximum):	∅150mm
Maximum frequency response:	5.5 Hz		

(c)

Fig. 2. (*Continued.*) AMADEUS phase I prototype gripper. (c) Specification.

moving parts in the finger itself) and the level of passive compliance. This lateral compliance enables the finger to deflect according to external physical constraints.
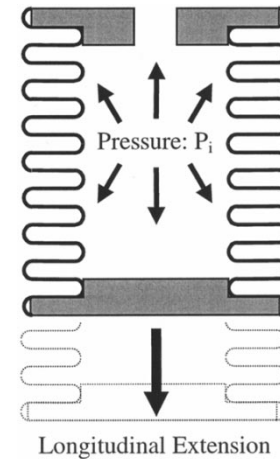
There is a minimum radius of curvature which can be produced by a finger. This radius is due to the wall thickness, convolution pitch, and the material used in the bellow actuators. The larger the maximum deflection required at the finger tip, the longer the normal length of the actuator must be. A series of plastic belts covered by neoprene sleeving supports the actuators along their length, reducing the risk of contact damage or buckling.
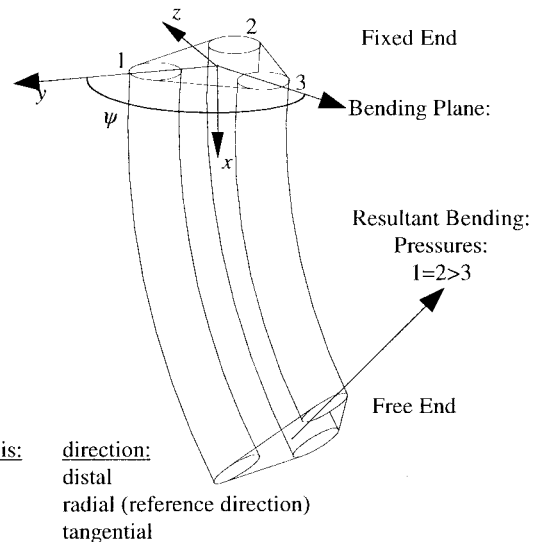
B. Palm Body

Three fingers are mounted in the palm of the gripper as a symmetrical triangle. Force closure in grasping is then more achievable with limited finger movement (future designs with more fingers may benefit from an offset opposable thumb). To allow the gripper to grasp a wide range of object sizes, the palm of the gripper incorporates knuckle joints. These joints are driven in concert from a small single central hydraulic cylinder via a simple linkage and provides each finger with 40° of angular rotation. This knuckle movement is sufficient to enable the finger tips to touch and grasp small objects (diameter (∅) 10 mm) or move apart so that larger objects (up to ∅ 150 mm) may be considered.

A small hydraulic cylinder (O.D. 22 mm), with both ports at the closed end, is used to drive the machined aluminum knuckle mechanism. Concentric guide bearing cylinders located about the body of the hydraulic cylinder minimize any side loads and reduce the risk of the mechanism jamming. This is achieved with no increase in the length of the piston assembly. Extension of the piston causes the gripper to flex by movement of a sliding rotary joint on each of the knuckle manifolds. Another rotational joint on each knuckle manifold is attached to the stationary outer bearing cylinder of the mechanism. Polyamide resin plain bearings and slide rings minimize the friction between all moving surfaces of the mechanism.

The knuckle joint alters the gripper configuration prior to object contact, whilst the individual finger motions are reserved for grasping and fine manipulation. Using phosphor-bronze bellows, a maximum of 20 mm of finger deflection minimizes permanent elastic damage to the bellows. Larger deflections would remove the need for a knuckle but require different bellows materials and is the subject of ongoing study. Large changes in position or orientation of grasped objects are performed by the arm or wrist onto which the gripper is mounted.

Longitudinal Extension

(a)

axis:	direction:
x	distal
y	radial (reference direction)
z	tangential

(b)

Fig. 3.   (a) Internal pressure causes mainly longitudinal extension. (b) Bending of flexible actuator caused by internal pressure differential.

C. Gripper Sensors

The modular finger tip (Fig. 4) contains a variety of sensors and interfaces with an attachment plate at the distal end of the active finger.

A small fifty-way push fit connector has been developed to split sensor feedback at the finger tip interface, allowing rapid substitution of the finger tip unit as required. A machined aluminum housing protects this connector and provides the basic form for the remainder of the finger tip. Water ingress into the housing is prevented by a nitrile O-ring seal. Sensor
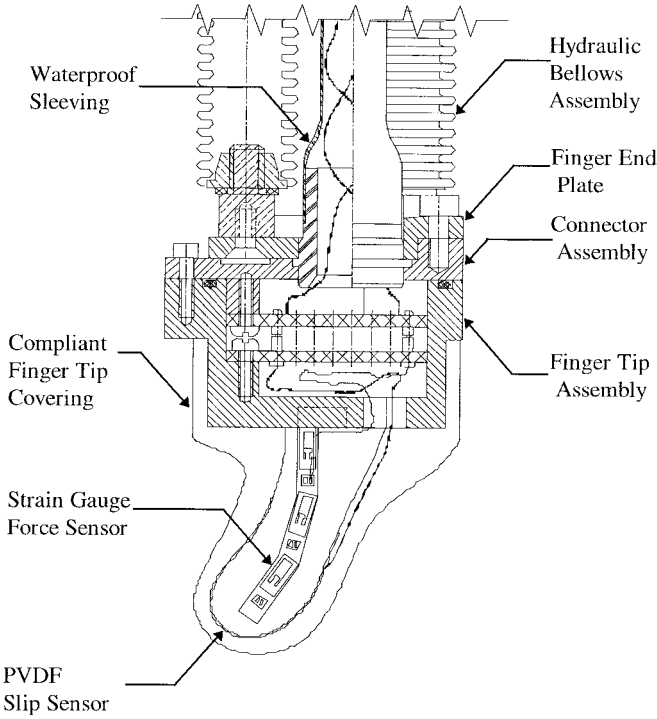
Fig. 4.   Detachable finger tip, with force and slip sensors.

Fig. 5.   Hysteresis of the proportional hydraulic control valves.

cabling is sleeved and routed between bellows along the central axis of each finger to the wrist.

The finger tip contact zone contains both a strain gauge arrangement for determining the magnitude and direction of contact forces and a PVDF piezoelectric film-based vibration (slip) sensor. The robustness of the sensors has been maximized by encapsulating them with a compliant silicon rubber compound, using a two-stage injection molding process.

The angle of the knuckle joint is measured by a rotary potentiometer driven from the knuckle mechanism via a rack and pinion. The potentiometer and drive assembly is housed in a robust oil-filled casing. Quad and O-ring seals prevent water ingress or oil leakage from this housing.

To meet user requirements for precision fingertip manipulation, the initial prototype employs force/slip sensors in the fingertips only. Course power grasps using finger sides and palm are also possible, although limited by the small fingertip deflection available. Although considered, no satisfactory solution for flexible, ambient pressure-independent force/slip sensors on finger walls has been achieved.

In the first prototype, no sensor is incorporated to measure fingertip position (although one has been identified). Initially, therefore, a calibrated model of the finger motion is used for closed-loop position control, driven by pressures measured from sensors within each tube [18].

D. Hydraulic System

The hydraulic system for the gripper uses a fixed displacement gear pump with pressure reducing pilot valve to maintain a system pressure of 30 bar. The pressure in each bellow actuator is controlled using a solenoid operated proportional
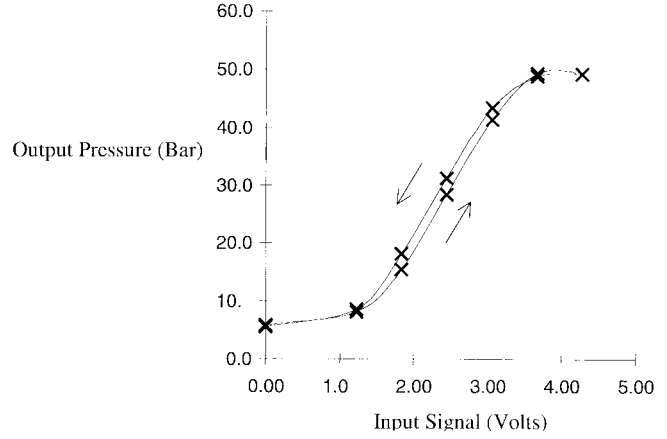
control valve with spring return. The static response of the proportional control valves is shown in Fig. 5.

The figure shows the response for a 50-bar supply pressure but the shape remains similar for the 30-bar pressure used with the initial gripper configuration. Due to valve leakage, the minimum pressure which can be delivered is 7.5 bar, and the fingers are usually operated above 12 bar to ensure that operation is within the central linear portion.

The control valve for the knuckle joint is a solenoid-operated three-position direction control valve with spring center alignment. This enables the flow to the knuckle joint to be either extended, retracted, or switched off. Fig. 6 shows the overall hydraulic arrangement, with associated computing.

III. STATIC MOTION CHARACTERISTICS OF THE FINGERS

A. Modeling Finger-Bending Plane Orientation Using Bending Moments

A direct approach to modeling the direction of motion of a finger can be obtained from the bending moment generated by each element of the finger. Fig. 7 is the view of a single finger viewed from above, directly along the axial (x) axis, in the finger base coordinate system. The three tubes in each finger are represented by the circles centered at the vertices of the equilateral triangle ABC. The triangle has sides of length a and height h. The relevant vector M_i identifies the magnitude and direction of the bending moment produced by the internal pressure in the ith element.

With the z and y axes positive in the direction shown, the resultant moment in the y direction can be expressed as

$$M_y = M_1 - M_2 \cos 60° - M_3 \cos 60° \qquad (1)$$

and in the z direction

$$M_z = -M_2 \sin 60° + M_3 \sin 60°. \qquad (2)$$

Using these two components, the magnitude of the resultant bending moment M_0 can be calculated from

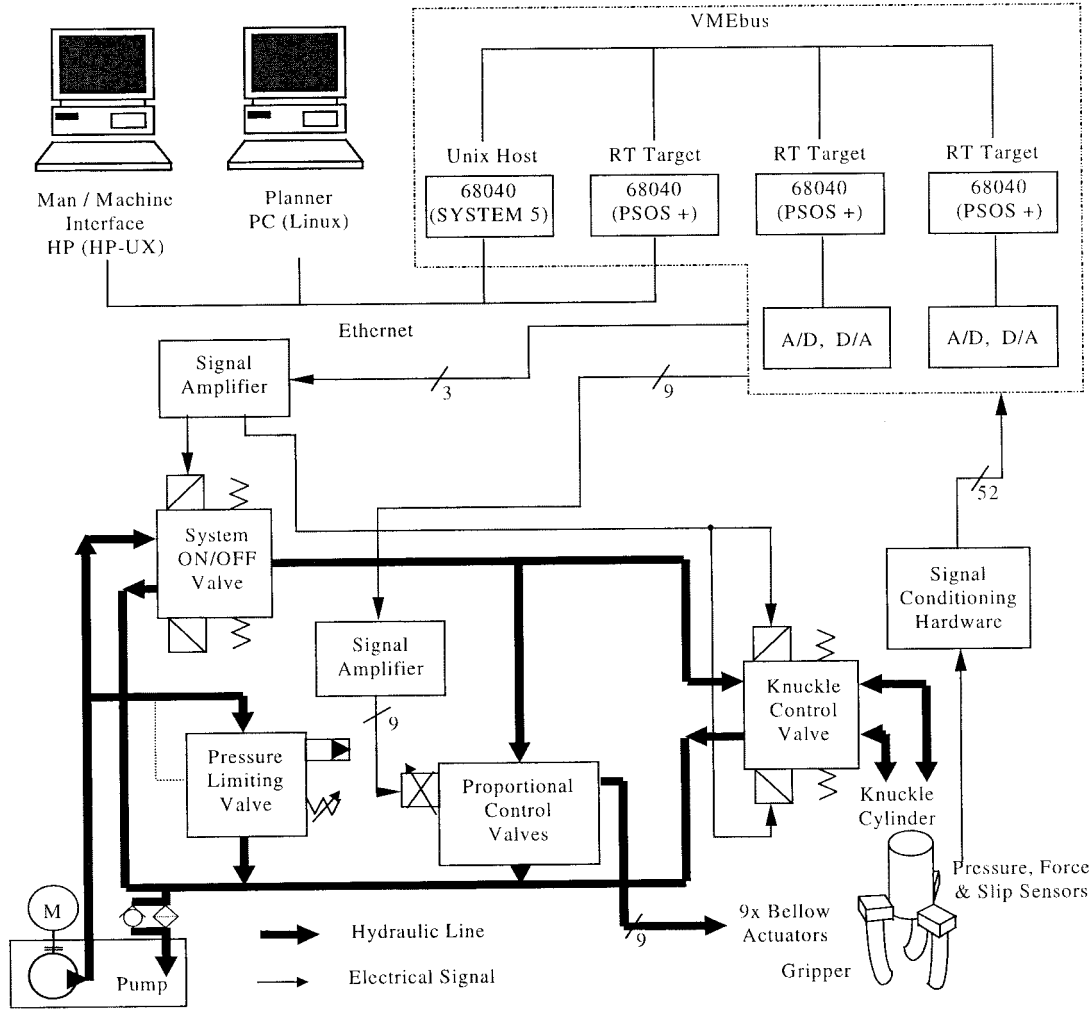$$M_0 = \sqrt{(M_z)^2 + (M_y)^2}. \qquad (3)$$

Fig. 6. Hydraulic and computer connectivity.

The orientation of the bending plane and the consequent direction of motion is determined using the relationship

$$\psi = \arctan\left(\frac{M_z}{M_y}\right). \tag{4}$$

B. Modeling Finger-Bending Plane Orientation Using Applied Pressures

Equation (4) identifies ψ in terms of the bending moments in the z and y directions, assuming that no out-of-plane forces are present.[1] However, the plane of bending and the direction of motion of the finger are ultimately controlled by the pressures in each tube.

The in-plane bending moment ΣM_{bi} and cross-plane bending moments ΣM_{ci} developed by the finger are given by

$$\sum_{i=1}^{3} M_{bi} = \sum_{i=1}^{3} P_i A_i \frac{2h}{3} \sin\psi_i \tag{5}$$

and

$$\sum_{i=1}^{3} M_{ci} = \sum_{i=1}^{3} P_i A_i \frac{2h}{3} \cos\psi_i. \tag{6}$$

[1] External forces not in the plane of the applied bending moment would produce a change in the direction of motion. Such force systems are not considered in this initial formulation.
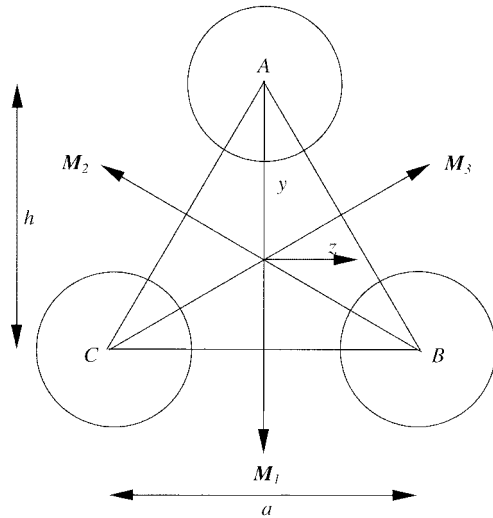

Fig. 7. Plan view of a single finger.

The resultant bending moment is thus

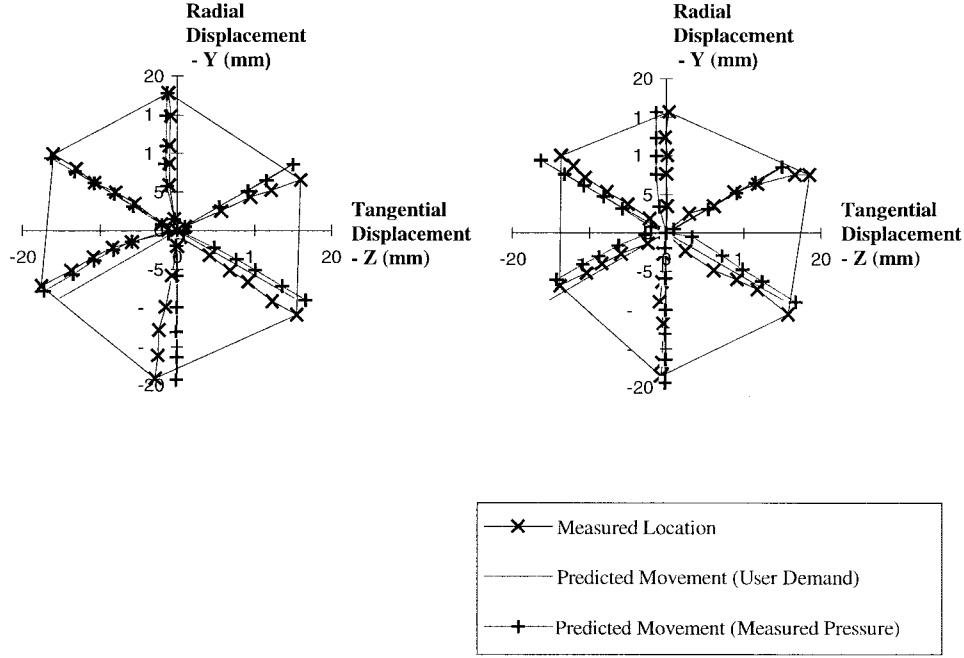$$M_r = \Sigma M_{bi} + \Sigma M_{ci}. \tag{7}$$

Fig. 8.   Measured and predicted finger motions with demanded and measured pressures.

Assuming the finger material is homogeneous and isotropic and that all tubes have the same area, the angle ψ is only a function of the relative magnitudes of the tube pressures P_1, P_2, and P_3. In the case where all three pressures are equal, regardless of the absolute magnitude of the forces, there will be no resultant bending moment $\boldsymbol{M}_r$ applied to the finger. When the pressure differential amongst all three tubes is nonzero, for the geometric layout in Fig. 7, the orientation of the finger-bending plane is given in terms of the tube pressures by the equation

$$\psi = \arctan\left(\frac{\frac{1}{2} - \left(\frac{P_1}{2\sum_{i=1}^{3} P_i} + \frac{P_3}{\sum_{i=1}^{3} P_i}\right)}{\frac{P_1 \sin 60°}{\sum_{i=1}^{3} P_i} - \frac{\sin 60°}{3}}\right). \qquad (8)$$

C. Experimental Validation of Static Finger Model

Using the gripper prototype of Section II, an open-loop experimental verification of the model in (8) was carried out for the six principal directions of finger movement. During this procedure, the usual finger tip was replaced with a small-diameter needle located along the centroidal (x) axis of the finger assembly. The location of the distal (i.e., free) end of this needle could be accurately ascertained by the use of a measuring block into a "world" measuring coordinate frame. This data was later transformed into the finger tip coordinate frame relative to the straight position of the finger tip. The location of the finger end and the actual pressures in each of the

three tubes was recorded for a series of pressure combinations about the known working zone of the finger.

The data can be divided into two sets.

1) The total pressure in the finger was the lowest required to achieve the displacement (i.e., one of the actuators was held at minimum pressure).
2) The total pressure in the finger was the highest possible to achieve the displacement (i.e., one of the actuators was held at a maximum pressure).

First, the measured position of the finger tip was plotted relative to the straight finger. Then the pressures demanded by the operator were used to produce a theoretical direction in which the finger was expected to move. Lastly, the pressures recorded in the system at each of the user demands were used to calculate a predicted direction of movement for the actual hydraulic pressures obtained from the proportional valves.

The results (Fig. 8) show a reasonable correlation between the theoretical direction of movement for a given set of pressure demands and the direction of movement actually obtained using the real gripper finger. At higher pressure demands, there was little difference between the demand and the actual pressure, but at lower pressures near the "elbow" in the proportional valve response the difference could be large. Other differences can be attributed to dissimilarities between nonisotropic bellows and torsional stresses introduced during assembly.

IV. CONTACT SENSOR PROCESSING

A. Force Measurements

The force sensing elements of the finger tip are 12 strain gauges attached to an inner skeletal structure [Fig. 9(a)] [19]. The covered sensor [Fig. 9(b)] consists of two parallel prongs,
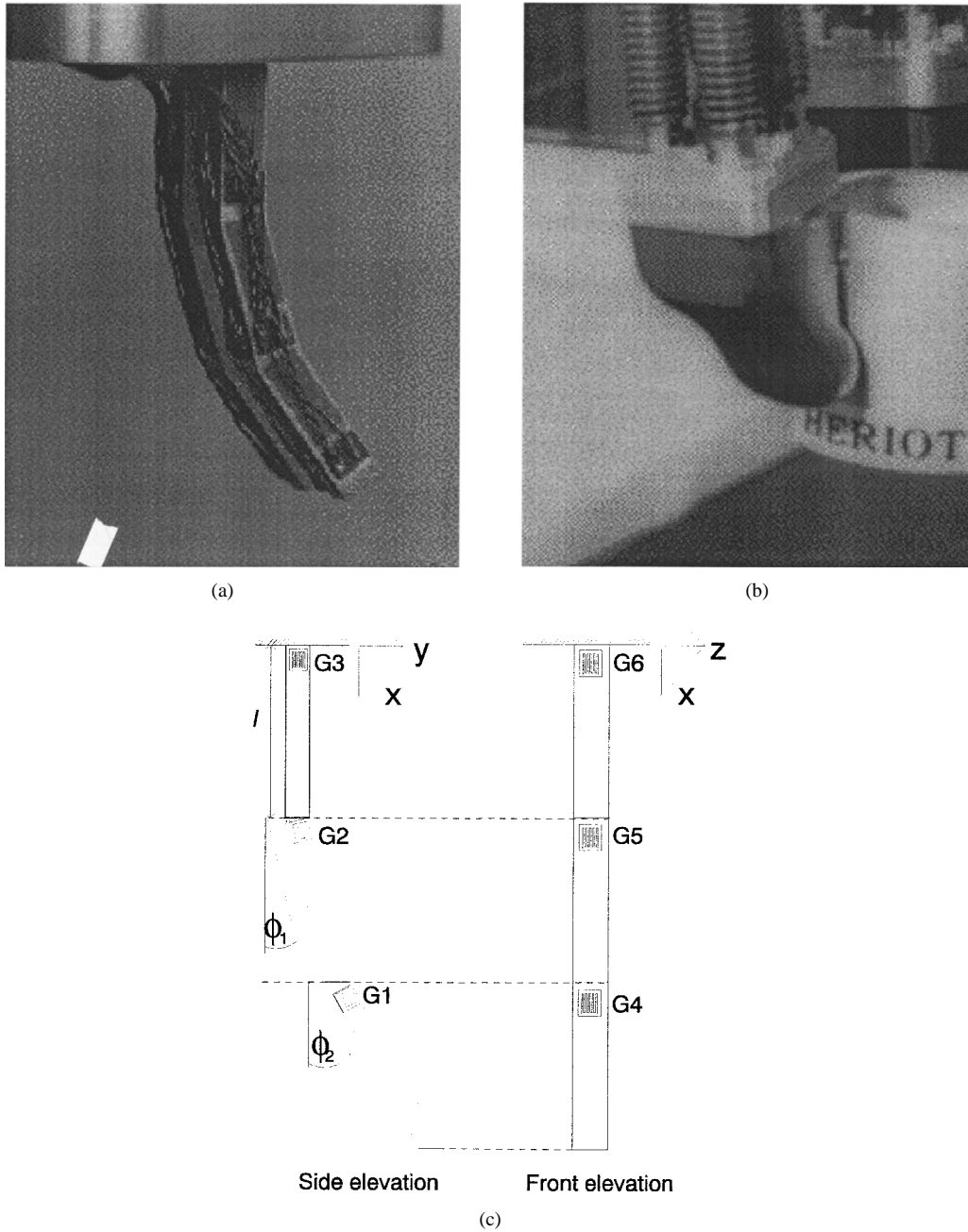
Fig. 9.   (a) Force sensor without covering. (b) Covered force sensor. (c) Distribution of strain gauges.

one of which is illustrated in Fig. 9(c). The forces obtained from the set of readings at each prong are averaged and the result corrected by a factor dependent on the compliant covering, obtained by calibration. Throughout, we assume point contact between fingertip and object, generally at the distal (bottom) end of the sensor. From Fig. 9, it is possible to derive the x, y, and z components of the distal end contact force in the sensor coordinate frame using the following.

Assume that a force is acting in the region of the distal end of the finger tip. Gauges 1–3 are sensitive in the z direction and gauge 6 solely in the y direction. Gauges 4 and 5 are sensitive mainly in the y direction but also partly in the x direction, according to the angles ϕ_1 and ϕ_2. For an arbitrary force $F = [f_x\ f_y\ f_z]$ acting at the distal end of the finger tip,

it can be shown that the readings from the strain gauge bridge circuits $R_1 \cdots R_6$ are

$$R_1 = K_1 l f_z \tag{9}$$
$$R_2 = K_2 l (1 + \cos(\phi_2 - \phi_1)) f_z \tag{10}$$
$$R_3 = K_3 l (1 + \cos\phi_1 + \cos\phi_2)) f_z \tag{11}$$
$$R_4 = K_4 l [\cos\phi_2 fy - \sin\phi_2 fx] \tag{12}$$
$$R_5 = K_5 l [(\cos\phi_1 + \cos\phi_2) fy - \sin\phi_1 fx] \tag{13}$$
$$R_6 = K_6 l (1 + \cos\phi_1 + \cos\phi_2)) f_y \tag{14}$$

and

$$F^2 = f_x^2 + f_y^2 + f_z^2 \tag{15}$$

where K_1–K_6 are calibration constants accounting for amplifier gains, beam stiffnesses, adherance of strain gauges, and

the conversion of force to an electrical signal, l is the length of each beam, and ϕ_1 and ϕ_2 are the beam angles relative to the sensor base coordinates. With six such equations, there is thus redundancy in solving for the three unknown forces.

As one might expect, the best measurements are those where the sensing element is furthest from the point of action of the force. Here, the bending moment, and hence the absolute value of the measured signal, is greatest. However, other measurements still contain useful information, and we can therefore exploit this redundancy to obtain force estimates which are more accurate than any individual measurement. A simple stochastic estimator based on a Kalman filtering approach, as outlined below, will perform such a task.

Assume that there are two measurements $\varepsilon_1(t_1)$ and $\varepsilon_2(t_2)$ of the same variable taken from different sensors a very short interval of time apart ($t_1 \cong t_2$), such that the variable value does not change between measurements. Furthermore, assume that each measurement contains the variable corrupted by additive, uncorrelated, zero mean, random noise with Gaussian probability density distribution and associated variance $\sigma_{\varepsilon 1}^2$ and $\sigma_{\varepsilon 2}^2$, respectively. Under these conditions, following Maybeck [20], a better estimate $\varepsilon_{12}(t_2)$ of the variable can be obtained as

$$\varepsilon_{12}(t_2) = \left[\frac{\sigma_{\varepsilon 2}^2}{\sigma_{\varepsilon 1}^2 + \sigma_{\varepsilon 2}^2} \right] \varepsilon_1(t_1) + \left[\frac{\sigma_{\varepsilon 1}^2}{\sigma_{\varepsilon 1}^2 + \sigma_{\varepsilon 2}^2} \right] \varepsilon_2(t_2) \quad (16)$$

or, in the update form used in filter implementation

$$\varepsilon_{12}(t_2) = \varepsilon_1(t_1) + \left[\sigma_{\varepsilon 1}^2 + \sigma_{\varepsilon 2}^2 \right] (\varepsilon_2(t_2) - \varepsilon_1(t_1)) \quad (17)$$

and

$$\sigma_{\varepsilon 12}^2 = \frac{\sigma_{\varepsilon 1}^2 \sigma_{\varepsilon 2}^2}{\sigma_{\varepsilon 1}^2 + \sigma_{\varepsilon 2}^2}. \quad (18)$$

Equation (17) says that the best possible estimate at time t_2 (in a mean, mode, maximum likelihood, or any other sense) is equal to the estimate at time t_1, plus a weighting applied to the difference between the original two estimates. The variance of the probability density distribution associated with the new estimate is lower than the variances of either of the two initial estimates, the implication being that the new estimate is necessarily better than either of the previous two. If there are more than two initial estimates, this may be extended without limit to provide ever more accurate estimates.

To implement such an estimator for the force sensor thus requires on-line calculation of the noise variances $\sigma^2 \varepsilon_i$ (where ε_i refers to measurements from particular strain gauge combinations). For this purpose, we make two assumptions.

1) The magnitude of the noise variance is linearly related to the magnitude of the measured signal—thus large signals have larger amounts of noise present (empirically confirmed).

2) The noise characteristics do not change over time, and the noise processes are zero mean with a Gaussian probability density distribution.

With these conditions, a normalized value of noise variance, σ_{Ni}^2 can be calculated from additional off-line calibration of particular strain gauge combinations. During calibration, repeated measurements are taken at each of several
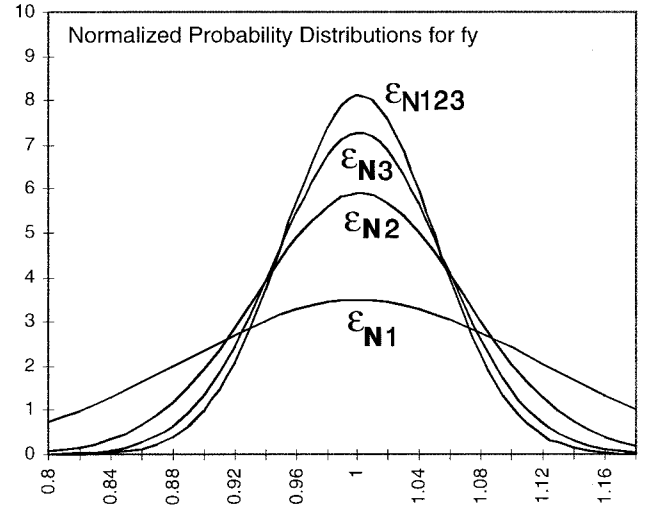

Fig. 10. Gaussian probability density distributions of normalized initial and normalized combined estimates.

TABLE I
ACTUAL AND THEORETICAL VARIANCES

Estimate	Actual σ_{Ni}^2	Theoretical σ_{Ni}^2
ε_{N1}	0.01309	–
ε_{N2}	0.00459	–
ε_{N3}	0.00301	–
ε_{N12}	0.00440	0.00340
ε_{N23}	0.00265	0.00181
ε_{N123}	0.00241	0.00160

applied forces, and the results are normalized using the known force value. The normalization is arranged to give a mean of unity (representing the signal, under the assumption of zero mean noise), and a normalized variance σ_{Ni}^2 (due to the noise alone). σ_{Ni}^2 is assumed not to change during system operation and is used on-line to calculate the actual noise variance for a particular measurement from the ith combination of strain gauges as

$$\sigma^2 \varepsilon_i = \varepsilon_i^2(t) \cdot \sigma_{Ni}^2. \quad (19)$$

This follows from the fact that a sample set, making up a Gaussian distribution with a mean of unity and variance σ^2, multiplied by a constant K, leads to a Gaussian distribution with a mean of K and variance $K^2 \sigma^2$.

Fig. 10 shows an example of three normalized probability density distributions ε_{N1}, ε_{N2}, ε_{N3}, with normalized noise variances σ_{N1}^2, σ_{N2}^2, σ_{N3}^2, obtained from calibration of three different strain gauge combinations in the y direction. It also shows the result of applying (17) and (18) to obtain a combined normalized estimate ε_{N123} with associated normalized noise variance σ_{N123}^2. It can be readily seen that the most accurate estimate ε_{N123} is an improvement on any of the three initial estimates, with smaller variance and greater probability of the measurement being closer to the true value.

Table I shows the normalized variances from the initial measurements, the calculated variances obtained from various strain gauge combinations in (17), and the variances which should theoretically have been found by (18).
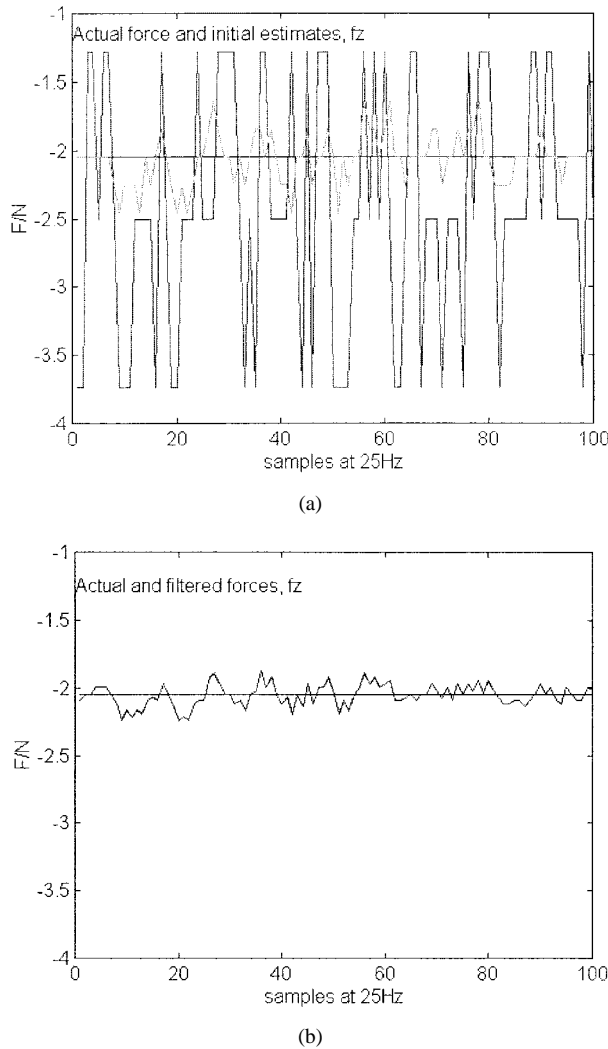
(a)

(b)

Fig. 11. (a) Plots of measurements $\varepsilon_1(t_1)$ and $\varepsilon_2(t_2)$ of a static applied force. (b) Plot of improved estimate $\varepsilon_{123}(t_2)$.

(a)

(b)

Fig. 12. (a) PVDF slip sensor prior to potting. (b) Plot of slip signal for different slip speeds using sensor testbed.

For illustration, Fig. 11(a) shows a sample set of the variations of two measurements $\varepsilon_1(t_1)$ and $\varepsilon_2(t_2)$ of a static applied force on the working gripper, and Fig. 11(b) shows the improved estimate $\varepsilon_{123}(t_2)$ obtained from the filter.

It is seen from Table I that the filter described does indeed provide an improvement in the quality of force data available from the sensor. However, the actual variances of the improved estimates are in all three cases higher than the theoretical variances calculated from (18). This is assumed to be due to violation of the two initial assumptions.

It should also be noted that the analysis here incorporates only the static estimation problem, and future work will include attempts to improve the quality of the force data when it is part of a control loop by incorporating dynamics into the filter.

B. Slip Measurement

Embedded 1 mm below the surface of the compliant covering of the sensor is a thin (52 μm) layer of piezoelectric film (PVDF) [Fig. 12(a)]. Piezoelectric film has the property 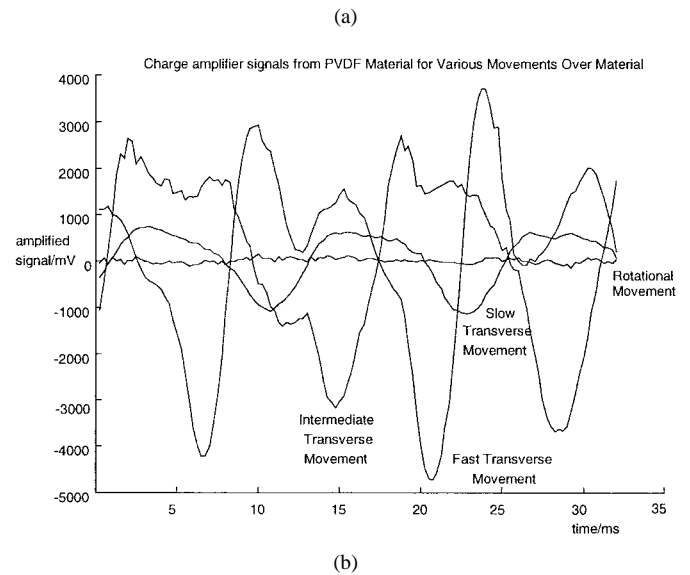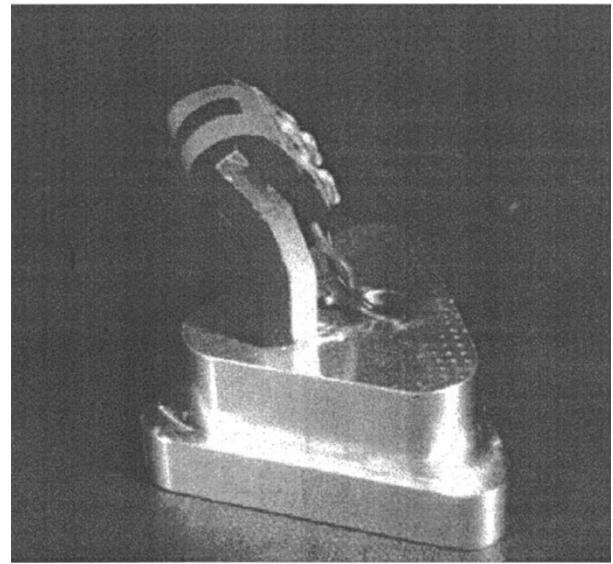that a charge is developed at its surface when it is subject to a deformation of any kind. This is a dynamic property in that once it stops deforming the charge built up on the surface quickly decays to zero. It is thus ideal for the measurement of transient phenomena but, on its own, unsuitable for measuring steady-state properties. Since film develops a (transient) charge at its surface when deformed, with suitable signal processing it has the ability to act as a vibration pickup.

When used as a slip sensor, the relative motion between two surfaces causes mechanical vibration in a direction normal to the plane of motion. The PVDF produces a voltage related to these vibrations and hence can indicate when a grasped object is slipping. Furthermore, the nature of the signal detected depends on the properties of the grasped object, the grasp force, the speed at which slip is taking place, and whether the motion is rotational or translational. Analysis of both the time- and frequency-domain signals should thus provide further information about the state of a grasp and any slippage, with a possible goal being the direct control of slippage during dextrous manipulation of an object.
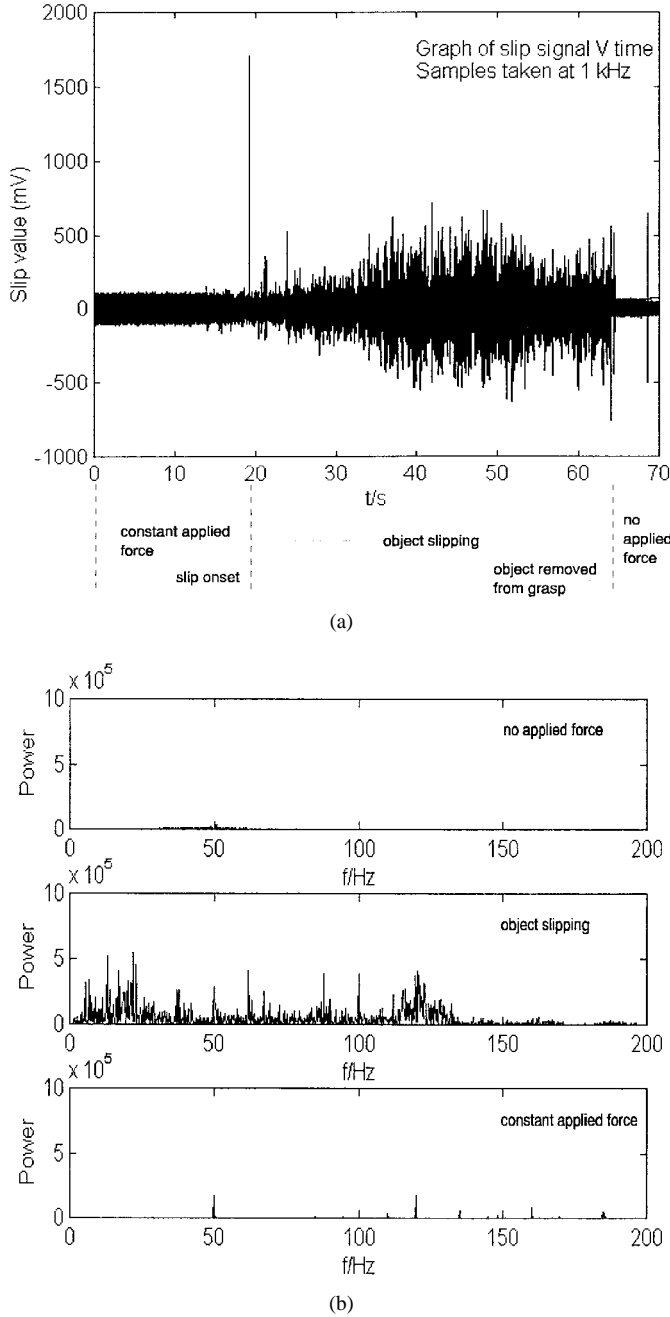
Fig. 13. Slip signals from prototype gripper *in situ*. (a) Time domain. (b) Frequency domain.

Tests of the sensor mounted on a sensor test rig have been carried out in the laboratory, and examples of time-domain plots for different slip speeds are shown in Fig. 12(b). Clearly, useful information concerning slip speed can be obtained from this data. Fig. 13 shows time- and frequency-domain plots of the sensor signal under different slipping conditions when mounted on the real robot. The additional energy present in the signal during slipping is clearly shown.

The performance of the slip sensors (in conjunction with the force data available from the force sensors) on each of the three finger tips is currently being evaluated in real grasping conditions. Initially, the slip sensors are being used simply to detect the onset of slippage and thus initiate a reflex reaction through the finger force control loops.

V. SYSTEM IDENTIFICATION OF FINGER DYNAMICS

As a precursor to the design of closed loop finger force control, identification experiments were carried out to make linear estimates of the system dynamics between pressure demand and force sensor readings. For this initial investigation, a single finger in contact with a steel plate was employed, pushing in one axis at one point in the workspace. Following [21], experiments used both off-line least squares (LS), and on-line recursive least squares (RLS) methods.

A. Model Structure

Both autoregressive (ARX) and autoregressive moving average (ARMAX) models, with exogenous input, were considered. For the former, the linear difference equation is

$$
\begin{aligned}
y(t) + a_1 y(t-1) + \cdots + a_{n_a} y(t-n_a) \\
= b_1 u(t-1) + \cdots + b_{n_b} u(t-n_b) + e(t) \quad (20)
\end{aligned}
$$

where $u(t)$ is the input signal, $y(t)$ the output, $e(t)$ is white noise, and n_a and n_b determine the model order. The vector of unknown parameters to be estimated is thus

$$
\Theta = [a_1 \quad a_2 \quad \cdots \quad a_{n_a} \quad b_1 \quad \cdots \quad b_{n_b}]^T. \quad (21)
$$

Shortening the notation gives

$$
\begin{aligned}
\boldsymbol{A}(z) &= 1 + a_1 z^{-1} + \cdots + a_{n_a} z^{-n_a} \\
\boldsymbol{B}(z) &= b_1 z^{-1} + \cdots + b_{n_b} z^{-n_b}
\end{aligned} \quad (22)
$$

and hence

$$
\boldsymbol{A}(z)y(t) = \boldsymbol{B}(z)u(t) + e(t). \quad (23)
$$

The ARMAX model is an extension to the ARX model. The difference is a moving average term applied to the noise, and models white noise which has been affected by some process dynamics. The model becomes

$$
\begin{aligned}
y(t) + a_1 y(t-1) + \cdots + a_{n_a} y(t-n_a) \\
= b_1 u(t-1) + \cdots + b_{n_b} u(t-n_b) + e(t) \\
+ c_1 e(t-1) + \cdots + c_{n_c} e(t-n_c) \quad (24)
\end{aligned}
$$

and with

$$
\boldsymbol{C}(z) = 1 + c_1 z^{-1} + \cdots + c_{n_c} z^{-n_c} \quad (25)
$$

the model is given by

$$
\boldsymbol{A}(z)y(t) = \boldsymbol{B}(z)u(t) + \boldsymbol{C}(z)e(t) \quad (26)
$$

and the parameter vector Θ becomes

$$
\Theta = [a_1 \quad \cdots \quad a_{n_a} \quad b_1 \quad \cdots \quad b_{n_b} \quad c_1 \quad \cdots \quad c_{n_c}]^T. \quad (27)
$$

ARX models are hence ARMAX models with $\boldsymbol{C}(z) = 1$. ARX models are appropriate when the system is deterministic, or when the noise is uncorrelated and white. ARMAX models are appropriate when white noise is passing through and hence colored by the process poles $\boldsymbol{A}(z)$ and the zeros in $\boldsymbol{C}(z)$.
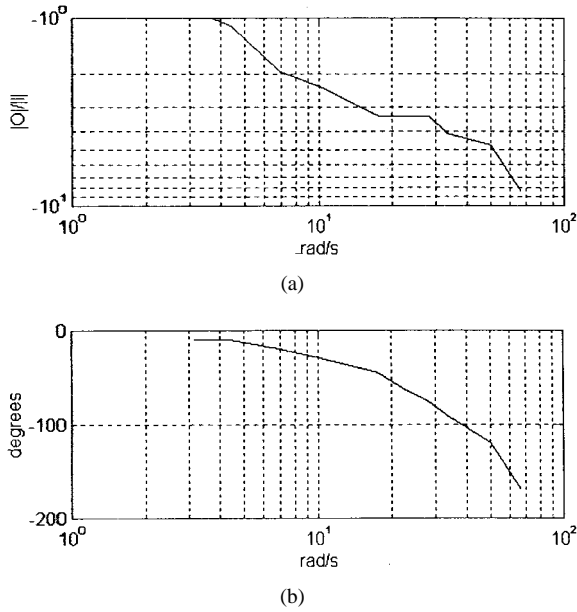
(a)

(b)

Fig. 14. Bode plot showing (a) measured force and (b) pressure demand frequency response for finger in contact with a rigid steel plate.

B. Model Selection and Validation

To determine the estimation accuracy of models, we define the mean square of the prediction error as a loss function. This provides a metric to compare estimated and real outputs and hence choose the model with the best performance.

The prediction error is given by

$$e(t, \Theta) = y(t) - \tilde{y}(t|\Theta) \tag{28}$$

where $\tilde{y}(t|\Theta)$ is the prediction of $y(t)$ given parameters Θ. The loss function is thus

$$V_N(\Theta) = \frac{1}{N} \sum_{t=1}^{N} \frac{1}{2} e^2(t, \Theta) \tag{29}$$

where N is the number of points.

C. Choice of Model Order

To determine model order, frequency response measurements were manually obtained using input sinusoids in the range 0.5–10.6 Hz (Fig. 14). Measured outputs were approximately sinusoidal, allowing estimates of gain and phase change from the waveforms.

While the amplitude curve is similar to a first-order system, with cut off somewhere between 1 and 10 Hz, the phase lag increases with frequency more rapidly than expected. This is in part due to a transport delay through the hydraulic proportional valves, illustrated by the step response in Fig. 15, obtained using the finger pressure transducers.

The delay is thus around 0.01 s. To avoid the need for an analog anti-alias filter, a sample interval of approximately 20 times the estimated system bandwidth (10 Hz) was chosen, giving 200 Hz. The delay in Fig. 15 then corresponds to two time steps with the chosen sample interval of 0.005 s.

From the above, we conclude that a first- or second-order model using one or two discrete time pole/zero combina-
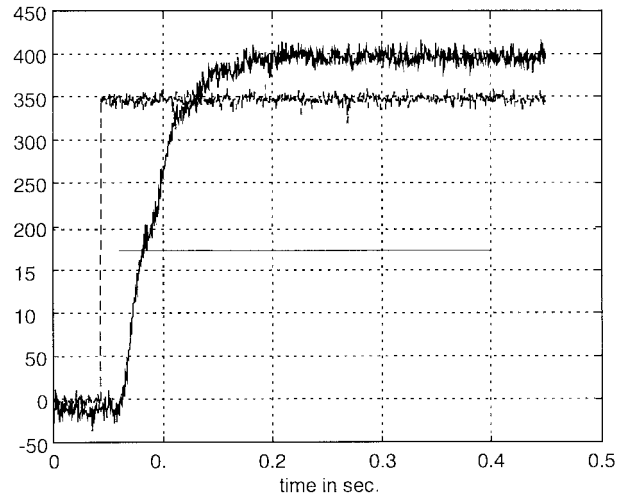

Fig. 15. Step response for one of the valves in the hydraulic system. Input (dashed line) is pressure demand and output (solid line) is pressure from transducer within the finger.
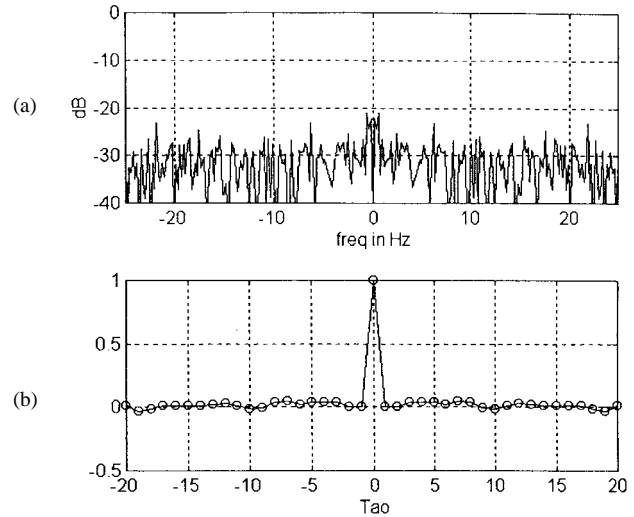

(a)

(b)

Fig. 16. (a) Spectrum and (b) autocorrelation of the noise in unfiltered force measurements.

tions, with a two-sample interval transport delay, makes an appropriate starting point for system identification.

D. Noise Considerations

Fig. 16 shows the spectrum and the autocorrelation function of signals obtained from a single strain gauge in the force sensor when the estimator of Section IV is not employed, and there is no pressure demand to the valves. This demonstrates the process and measurement noise in combination, and illustrates two points.

1) There is significant noise energy outside the bandwidth of the finger, which could be removed in the frequency domain prior to estimation. Given the absence of an analog anti-alias filter and the high sampling rate, this is to be expected.

2) The noise is not correlated with itself, except for very small values of τ, and can therefore be considered random.

TABLE II
ESTIMATED MODELS USING LEAST SQUARE FOR DIFFERENT DATA AND MODEL STRUCTURE

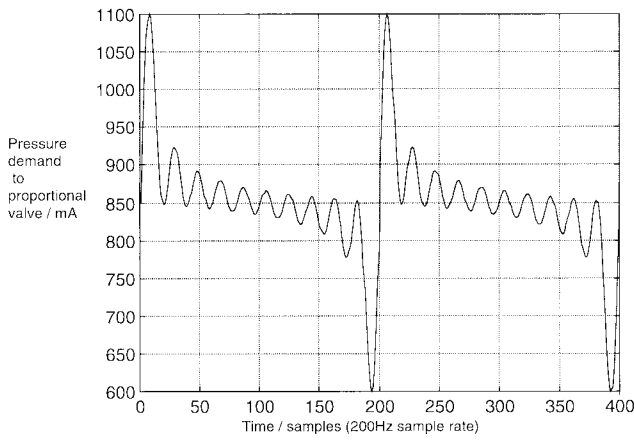| Input Data S_1 or S_2	Model [denom. coeffs, num. coeffs, delay]	A $A(z) = 1 + a_1 z^{-1} + \ldots + a_{n_a} z^{-n_a}$	B $B(z) = b_1 z^{-1} + \ldots + b_{n_b} z^{-n_b}$	Loss Function
S_1	[1 1 2]	1, -0.9884	0, 0, -0.0667	653
S_2	[2 2 2]	1, -1.9258, 0.9432	0, 0, 0.2382, -0.2687	56.4
S_1	[2 2 2]	1, -1.8732, 0.8996	0, 0, 0.1950, -0.2276	27.62
S_1	[3 2 2]	1, -2.4705, 2.0620,-0.5804	0, 0, 0.1011, -0.1200	16.75
S_1	[4 4 2]	1, -2.8040, 3.3595, -2.1409, 0.6073	0, 0, -0.3256, 0.5611, -0.0449, -0.2394	8.047
S_1	[2 2 10]	1, -1.7687, 0.8070	0,0,0,0,0,0,0,0,0,0, -0.1526, 0.07	24.69

Fig. 17. Excitation signal S_1: sum of frequencies in the range 1–10 Hz.

Fig. 18. One second of excitation signal S_2: bandpass random white noise, 0.3–10 Hz.

Initial attempts at estimation using an ARX and ARMAX models with raw force data produced very poor models, with very large values of prediction error. To address this and reduce the noise, for the experiments in this section only, a second-order low-pass Butterworth filter with cut off $f_c = 9$ Hz was used, adding two poles at $z = 0.8021 \pm j0.1648$ and two zeros at $z = -1$ with the 200 Hz sampling frequency. This substantially reduced the magnitude of the noise present, allowing estimation to proceed.

Finally, since the noise is apparently random, we chose an ARX model for estimation purposes (i.e., set $C(z) = 1$).

E. Off-Line System Identification Using Least Squares

Initially we measured the performance of various ARX LS estimators, with two different input signals $u(t)$ to excite the process.

Signal S_1 is 400 samples at 200 Hz (i.e., 2 s) of data containing a sum of frequencies from 1 to 10 Hz, inclusive, at 1-Hz intervals (Fig. 17). Input values to the proportional valve are in the range 600–1100 mA, centered on a mean operating value of 850 mA. The other two valves are held constant at 1100 mA. The finger was pushing in contact with a rigid steel plate.

Excitation signal S_2 is 4000 samples at 200 Hz (i.e., 20 s) of data containing a bandpass-filtered random signal, using cutoff frequencies of 0.3 and 10 Hz (Fig. 18).
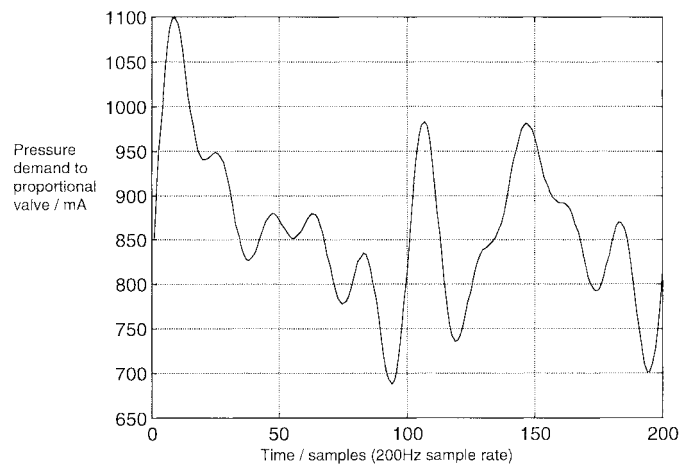
Model structures using 1–4 nonzero coefficients in $A(\,)$ and $B(\,)$ and time delays of 2 and 10 sample intervals were employed. In the [222] notation of Table II, the entries give the [n_a coefficients, $n_b - 1$ coefficients, n_k delay] values in the ARX model. The loss function was calculated as per (29). In this section and Section V-F below, a second-order Butterworth filter cut off 9 Hz was employed with the measured force data. This adds two poles at $z = 0.8021 \pm j0.1648$ and two zeros at $z = -1$ and removes high-frequency sensor noise out with the finger bandwidth. The filter is not incorporated in the estimator structure.

Models estimating more coefficients clearly give better performance, but at the computational cost of estimating these extra parameters. Based on this test, a reasonable compromise would involve two denominator coefficients, one numerator, and two delays (i.e., $[2, 2, 2]$) for the best fit at least cost.

F. On-Line System Identification Using Recursive Least Squares

With fixed process dynamics, off-line estimation can produce model parameters adequate for fixed gain control system design. However, process dynamics can change on-line, in which case parameters will change. Recursive estimation provides the means to monitor this.
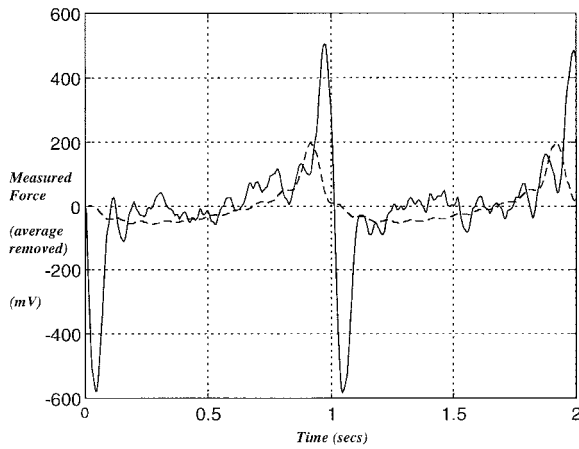
Fig. 19.   Modeled (dashed line) and measured (solid line) force versus time for a one-coefficient model [112] using ARX RLS with S_1 input at 200 Hz.
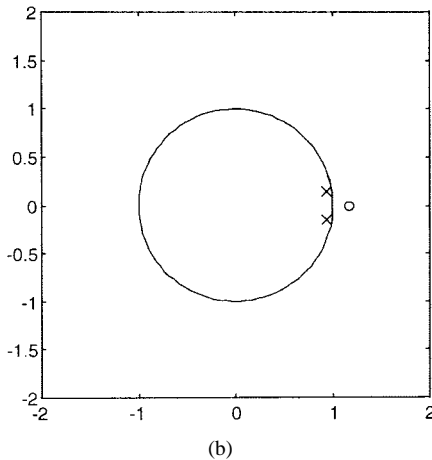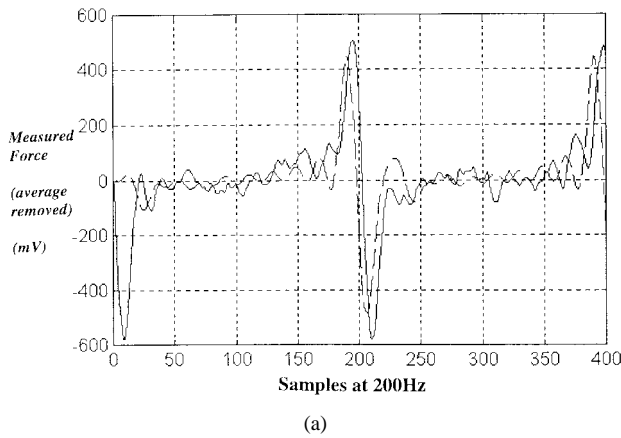

(a)

(b)

Fig. 20.   (a) Modeled (dashed line) and measured (solid line) force versus time for a two-coefficient model [222] using ARX RLS with S_1 input at 200 Hz. (b) z-plane pole-zero diagram for the same condition.

(a)

(b)

Fig. 21.   (a) Modeled (dashed line) and measured (solid line) force versus time for a two-coefficient model [2210] with ten samples of transport delay. ARX RLS with S_1 input at 200 Hz. (b) z-plane pole-zero diagram for the same condition.
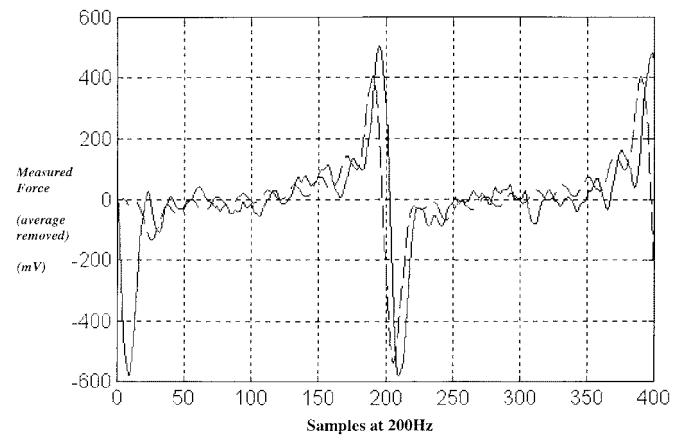
Fig. 22.   Modeled (dashed line) and measured (solid line) force versus time for a four-coefficient model [433] using ARX RLS with S_1 input at 200 Hz.

Initially we study only the convergence and modeling errors of recursive estimation for a single finger position on a laboratory test rig. Further experiments will be required throughout the finger work envelope, to establish the extent of any changes.

Figs. 19–22 show modeled and measured signals from a force sensor plotted against time. As above, the force sensor was in contact with a rigid steel plate. Experiments were tried with and without the Butterworth filter in Section V-E. Filtered measurements from the sensor in contact with the rigid steel plate with fixed pressure demand 1100,1 100 850 were also taken and averaged. This average value has been subtracted

TABLE III
SUMMARY OF ARX RLS ESTIMATOR PARAMETERS AND ERRORS FOR VARIOUS FINGER MODELS

Model	Filter	A			B			Loss Funct.
		Param	Value	σ_A	Param	Value	σ_B	
[1,1,1]	no	a_0	1	0	b_0	0	0	1.974e+004
		a_1	-0.713	0.0345	b_1	-0.279	0.0956	
[1,1,2]	no	a_0	1	0	b_0	0	0	1.918e+004
		a_1	-0.6939	0.0343	b_1	0	0	
					b_2	-0.3753	0.0952	
[1,1,3]	no	a_0	1	0	b_0	0	0	1.875e+004
		a_1	-0.667	0.0348	b_1	0	0	
					b_2	0	0	
					b_3	-0.4869	0.0962	
[2,2,1]	no	a_0	0	0	b_0	1	0	1.671e+004
		a_1	2.9475	0.5260	b_1	-0.4469	0.0479	
		a_2	-3.3422	0.5306	b_2	-0.2186	0.0458	
[2,2,2]	no	a_0	1	0	b_0	0	0	1.62e+004
		a_1	-0.4151	0.0480	b_1	0	0	
		a_2	-0.1994	0.0454	b_2	3.1914	0.5451	
					b_3	-3.7282	0.5565	
[2,2,3]	no	a_0	1	0	b_0	0	0	1.577e+004
		a_1	-0.3817	0.0484	b_1	0	0	
		a_2	-0.1754	0.0453	b_2	0	0	
					b_3	3.1750	0.5650	
					b_4	-3.8776	0.5862	
[2,2,2]	9Hz	a_0	1	0	b_0	0	0	27.62
		a_1	-1.8732	0.0117	b_1	0	0	
		a_2	0.8996	0.0117	b_2	0.1950	0.0221	
					b_3	-0.2276	0.0225	
[2,2,3]	9Hz	a_0	1	0	b_0	0	0	26.63
		a_1	-1.8534	0.0124	b_1	0	0	
		a_2	0.8814	0.0122	b_2	0	0	
					b_3	0.1856	0.0231	
					b_4	-0.2272	0.0238	
[3,2,3]	9Hz	a_0	1	0	b_0	0	0	16.35
		a_1	-2.4448	0.0387	b_1	0	0	
		a_2	2.0240	0.0731	b_2	0	0	
		a_3	-0.5668	0.0359	b_3	0.0993	0.0189	
					b_4	-0.1234	0.0198	
[3,3,3]	9Hz	a_0	1	0	b_0	0	0	15.39
		a_1	-2.3841	0.0395	b_1	0	0	
		a_2	1.9541	0.0723	b_2	0	0	
		a_3	-0.5522	0.0723	b_3	-0.4609	0.1123	
					b_4	1.0338	0.2294	
					b_5	-0.6237	0.1231	
[4,3,3]	9Hz	a_0	1	0	b_0	0	0	8.222
		a_1	-2.8094	0.0368	b_1	0	0	
		a_2	3.3652	0.0926	b_2	0	0	
		a_3	-2.1399	0.0893	b_3	-0.3287	0.0824	
		a_4	0.6059	0.0327	b_4	0.7788	0.1683	
					b_5	-0.4961	0.0903	

from the force data, effectively ac coupling the measurements. Throughout, the signal S_1 is used as input.

For estimation, models with up to four nonzero numerator or denominator coefficients with two- or ten-interval transport delays were tried. Table III summarizes the resulting $A()$ and $B()$ parameter values, their standard deviations σ, and the loss function for prediction error in each case.

The Butterworth filter reduces the variability of paramaters by a factor of 4, and the loss function by a factor of 1000, and hence performs a useful role. As with the LS results, models estimating more coefficients generally have lower loss functions. The model $[1, 1, 1]$ with only one numerator and denominator coefficient has the worst σ for parameter variation. The two-coefficient model with a two-sample intervals delay

$[2, 2, 2]$ is again a good compromise, identifying the same parameters as with the LS estimator. However, the system is nonminimum phase, with a zero outside the unit circle. Using pole placement, or other pole/zero cancellation design methods for control, will therefore be a risky endeavor, in the event of inexact cancellation. Interestingly, introducing the ten-sample delay into the two-coefficient model produces a pole-zero plot which is minimum phase.

G. Further Work

The results have shown that adequate dynamic modeling performance for the finger can be obtained when estimating only two coefficients in numerator and denominator, and that

parameters converge to sensible values using ARX RLS. It remains to estimate similar models across a range of positions and directions of push in the workspace to ascertain the extent to which the finger dynamics change. These models will be helpful in further consideration of force control system design.

VI. Conclusions

We have described our first attempt at developing a prototype dextrous underwater gripper using continuum actuators for fingers with integrated force and slip sensors. Approaches to sensor signal processing, static modeling of finger position, and on-line estimation of finger force dynamics have been presented. This work forms part of a portfolio of activity from phase I of the AMADEUS project [22]–[24]. Related work included active control of finger vibration [25], coordinated finger control for grasping and manipulation [26], tele-assistant blind grasping for operation in reduced or zero visibility [27], and man–machine interface design [28].

The prototype produced in phase I successfully carried out precision fingertip grasping and manipulation of rigid and compliant objects in the laboratory test tank and involved the complex integration of a range of mechanical, electrical, and computing subsystems. Several critical factors were identified, including the material properties of the bellows, the detail of the finger design to prevent buckling, improved design of the fingertip shape, corrosion engineering of dissimilar metals in the gripper, and system integration issues, including well-defined interfaces and software compatibility.

Phase II of the project is currently underway, with an extended consortium involving benthic scientists and marine geologist users [29]. An improved gripper and finger design is being mounted on a conventional hydraulic underwater manipulator for in-water trials deployed from an ROV toolskid. The new design incorporates video and acoustic sensors in the gripper palm. A future publication will report on the complete system performance, including a marine science user's perspective on effectiveness and usability.

Continuum actuators have much to offer for subsea use, and these early activities have shown promise. The basic finger design is scaleable, limited only by the need to support its own (in water) weight, and the choice and availability of appropriate bellows materials. Other subsea applications as an inspection and as a propulsion device are currently under investigation [30].

Acknowledgment

References

[1] AMADEUS Phase II WP100 Deliverable, "Scientific and technical requirements," Ocean Systems Lab., Dept. Computing & Electrical Engineering, Heriot-Watt Univ, Edinburgh, Dec. 1996, 82 pages.
[2] H. Yoshinada, T. Yamazaki, and T. Suwa, "Seawater hydraulic actuator system for underwater manipulator," in *Fifth Int. Conf. Advanced Robotics*, Pisa, Italy, 1991, pp. 1130–1335.
[3] J. B. C. Davies, "A flexible motion generator," Ph.D. dissertation, Dept. Mech. and Chemical Eng., Heriot-Watt University, Edinburgh, U.K., 1996.
[4] *Proc. IEEE Int. Conf. Robotics and Automation*, Nagoya, Japan, May 21–27 1995, Sessions WAI-12 WAII-12 WPI-12 WPII-12.
[5] J. P. Trevelyan, P. D. Kovesi, M. Ong, and D. Elford, "ET: A wrist mechanism without singular positions," *Int. J. Robot. Res.*, vol. 4, no. 2, pp. 71–85, 1986.
[6] A. Hemani, "Design of light weight flexible robot arm," in *Proc. Robots 8*, Detroit, MI, June 4–7, 1984, vol. 2, pp. 16-22–16-40.
[7] K. Suzumori, S. Likura, and H. Tanaka, "Applying a flexible microactuator to robotic mechanisms," *IEEE Contr. Syst. Technol.*, pp. 21–27, Feb. 1992.
[8] S. Hirose, *Biologically Inspired Robots*. Oxford, U.K.: Oxford Univ., 1993.
[9] D. G. Caldwell, G. A. Medrano-Cerda, and M. Goodwin, "Characteristics and adaptive control of pneumatic muscle actuators for a robotic elbow," in *Proc. 1994 IEEE Int. Conf. Robotics & Automation*, San Diego, CA, May 8–13, pp. 3558–3563.
[10] G. Immega and K. Antonelli, "The KSI tentacle manipulator," in *Proc. 1995 IEEE Int. Conf. Robotics & Automation*, Nagoya, Japan, May 21–27, pp. 3149–3154.
[11] J. B. C. Davies, "An alternative robotic proboscis," in *Proc. NATO Advanced Research Workshop on Traditional and Non-Traditional Robots*, Maratea, Italy, Aug. 28–Sept. 2, 1989, pp. 49–55.
[12] ——, "Elephants trunks: An unforgettable alternative to rigid mechanics," *Industrial Robot*, vol. 18, pp. 29–30, 1991.
[13] ——, "Dextrous manipulator for complex objects," in *Proc. Fifth World Conf. Robotics Research*, Cambridge, MA, Sept. 27–29, 1994, pp. 17-15–17-28.
[14] D. M. Lane, J. B. C. Davies, J. Sneddon, D. J. O'Brien, and G. C. Robinson, "Aspects of the design and development of a subsea dextrous grasping system," in *IEEE OCEANS '94*, Brest, France, Sept. 13–16, 1994, vol. II, pp. 174–181.
[15] J. B. C. Davies and G. Robinson, "A flexible dexterous gripper," in *Proc. SPIE Int. Conf. Robotics Research*, Cambridge, MA, Sept. 1995.
[16] J. Napier, "The prehensile movements of the human hand," *J. Bone Joint Surg.*, vol. 38B, pp. 902–913, 1956.
[17] T. Schilling, "Design considerations for underwater robotics systems," in *Ocean Resources, vol. II*, A. D. and M. Champ, Eds. Dordrecht, The Netherlands: Kluwer, 1990, pp. 11–17.
[18] G. Bartolini, D. M. Lane, J. B. C. Davies, G. Casalino, G. Cannata, and G. Veruggio, "AMADEUS: Advanced manipulator for deep underwater systems," in *CEC Second MAST Days and EUROMAR Market*, Sorrento, Italy, Nov. 7–10, 1995, pp. 991–10006.
[19] D. J. O'Brien and D. M. Lane, "The design, modeling and analysis of a strain gauge-based force sensor for subsea applications using the structural stiffness method," in *Proc. 7th Int. Conf. Advanced Robotics*, San Feliu de Guixols, Spain, Sept. 20–22, 1995, pp. 177–182.
[20] P. S Maybeck, *Stochastic Models, Estimation and Control*. New York: Academic, 1979, vol. 1.
[21] P. E. Wellstead and M. B. Zarrop, *Self Tuning Systems—Control and Signal Processing*. New York: Wiley, 1991.
[22] D. M. Lane, "The AMADEUS dexterous underwater grasping system," *Int. J. Syst. Sci.*, vol. 29, no. 4, pp. 445–454, Apr. 1998.
[23] G. Robinson, J. B. C. Davies, and E. Seaton, "Mechanical design, operation and direction prediction for the AMADEUS gripper system," *Int. J. Syst. Sci.*, vol. 29, no. 4, pp. 455–470, Apr. 1998.
[24] D. J. O'Brien and D. M. Lane, "Force and explicit slip sensing for the AMADEUS underwater gripper," *Int. J. Syst. Sci.*, vol. 29, no. 4, pp. 471–484, Apr. 1998.
[25] G. Bartolini, M. Coccoli, and A. Ferrara, "Vibration damping & second order sliding modes in the control of a single finger of the AMADEUS gripper," *Int. J. Syst. Sci.*, vol. 29, no. 4, pp. 497–512, Apr. 1998.

[26] D. Angelleti, G. Cannata, and G. Casalino, "The control architecture of the AMADEUS gripper," *Int. J. Syst. Sci.*, vol. 29, no. 4, pp. 485–496, Apr. 1998.

[27] D. M. Lane and M. Pickett, "Task planning for dexterous manipulation using blind grasping tele-assistance," *Int. J. Syst. Sci.*, vol. 29, no. 4, pp. 513–528, Apr. 1998.

[28] G. Veruggio, R. Bono, and P. Virgili, "The AMADEUS man machine interface," *Int. J. Syst. Sci.*, vol. 29, no. 4, pp. 529–538, Apr. 1998.

[29] D. M. Lane, J. B. C. Davies, G. Casalino, G. Bartolino, G. Cannata, G. Veruggio, M. Canals, and C. Smith, "AMADEUS: Advanced manipulator for deep underwater sampling," *Special Issue of the IEEE Robotics and Automation Society Magazine*, Dec. 1997.

[30] J. B. C. Davies, D. M. Lane, G. C. Robinson, D. J. O'Brien, M. Pickett, M. Sfakiotakis, and B. Deacon, "Subsea applications of continuum of robots," in *Proc. Underwater Technology 98*, Apr. 15–17, 1998, Tokyo, Japan.

Graham Robinson graduated from Heriot-Watt University, Edinburgh, U.K., in 1991 in computer-aided mechanical engineering and received the M.Sc. degree in bioengineering from Strathclyde University, U.K., in 1992, where he designed an external fixator for reduction of fractures of the distal radius. He is currently working toward the Ph.D. degree on the design of continuum robots and their application to dextrous grasping activities at Heriot-Watt University.

In 1993, he returned to Heriot-Watt University to work on the AMADEUS dextrous robot end-effector project. Here his main responsibility is the mechanical design of the gripper.

David M. Lane received the B.Sc. degree in 1980 in electrical and electronic engineering and the Ph.D. degree in 1986 for work on subsea robotics.

He is a Professor in the Department of Computing and Electrical Engineering at Heriot-Watt University, Edinburgh, U.K. His research interests involve using advanced technology in the ocean, embracing tethered and autonomous underwater vehicles and subsea robotics. He is currently the coordinator of the MAST-III project AMADEUS, and principle Heriot-Watt investigator on the collaborative CEC programs MAST III ARAMIS, MAST II AMADEUS Phase I, and for the ESPRIT III UNION Basic Research Action, now finished. He also holds grants for several U.K. Government and industry funded projects, involving underwater robotics for North Sea oil and gas exploration and production. He was peviously involved in the EUREKA EU191 Advanced Underwater Robots AUV program. He has worked in the U.K. Defence Industry as a Development Engineer and in the Offshore industry on the operations and maintenance of manned underwater vehicles for inspection and survey.

Dr. Lane is a Chartered Engineer in the U.K. He is a Member of the Institution of Electrical Engineers (IEE). He was the initial chairman of the European MAROBOT special interest group on Subsea Robotics, is a member of IEE Professional Group B3, Intelligent Automation and Robotics, and the UK Society for Underwater Technology Underwater Robotics Group. He is Associate Editor of *International Journal of Systems Science* and has recently acted on numerous Program Committees for IEEE Oceanic Engineering and Robotics & Automation Societies, including organizing special sessions at the annual international conferences.

J. Bruce C. Davies received the degree in mechanical engineering from the University of Manchester Institute of Science and Technology in 1970 and the M.Sc. and Ph.D. degrees from Heriot-Watt University, Edinburgh, U.K., in 1982 and 1996, respectively.

After graduating from the University of Manchester, his first appointment was as Graduate Development Engineer with British Leyland Tractor Division. In 1975, now a Senior Development Engineer (Tractors), he left to join Balmore Hydraulics, Ltd., initially as Chief Engineer, but from 1977 to 1982 as Technical Director. During this period, the company expanded into the design and manufacture of equipment for the Offshore Oil and Petrochemical Processing Industries. In 1982, he moved to Heriot-Watt University, Edinburgh, U.K., as a Lecturer in Mechanical Engineering. He is currently a Senior Lecturer in the Department of Mechanical and Chemical Engineering at Heriot-Watt with research interests in the areas of design and manufacture, underwater robotics, and medical engineering.

Desmond J. O'Brien received the B.E. degree in electrical engineering and microelectronics in 1990 and the M.Eng.Sc. degree in 1992 from University College Cork, Ireland, where his research interests included discrete-time simulation of manufacturing processes and the design and control aspects of electromechanical systems for CNC machines. He is currently working toward the Ph.D. degree at Heriot-Watt University, Edinburgh, U.K.

He joined the Ocean Systems Laboratory of the Department of Computing and Electrical Engineering at Heriot-Watt University in 1993, where he is currently a Research Associate. His current research interests include the development of sensors and sensing subsystems for underwater manipulators and the control of flexible actuators and underwater robots.

Jim Sneddon received the M.Eng. degree in computing and electrical engineering from Heriot-Watt University, Edinburgh, U.K.

He currently works for IBM UK carrying out contract software development for business and commercial applications. Prior to joining the Ocean Systems Laboratory, Department of Computing and Electrical Engineering, Heriot-Watt University, he worked on the development of state of the art ship stabilizers and marine controls for Brown Brothers plc, Edinburgh.

Euan Seaton received the B.Eng. degree in mechanical engineering from Heriot-Watt University, Edinburgh, U.K.

Anders Elfstrom received the M.Sc. degree in digital systems engineering from Heriot-Watt University Edinburgh, U.K.

He currently works in industry in Sweden.